Available online at www.sciencedirect.com
SCIENCE DIRECT®
International Journal of Thermal Sciences 45 (2006) 681–690
International Journal of Thermal Sciences
www.elsevier.com/locate/ijts

Numerical and experimental investigation on the thermofluid fields induced by a pen-like atmospheric nonthermal plasma torch

T.H. Ko [a,*] C.M. Liu [a], Y. Matsuo [b], S. Ono [b], S. Teii [a,b]

[a] *Lunghwa University of Science and Technology, Taiwan*
[b] *Musashi Institute of Technology, Tokyo, Japan*

Received 18 April 2005; received in revised form 26 October 2005; accepted 26 October 2005
Available online 5 December 2005

Abstract

The present paper carried out the numerical simulation and experimental study of the thermofluid fields induced by a pen-like atmospheric nonthermal plasma torch, which is a very simple device to produce atmospheric plasma and has been successfully applied for surface treatment to improve the hydrophilic properties of plastic film and polyethylene. The device consists of a small cylindrical stainless steel pipe with 6.5 mm diameter and 170 mm length inserted into a ceramic tube as the inner electrode. A ring outer electrode made of stainless steel is fixed at near the edge of the ceramic. The 13.56 MHz RF power was applied between the two electrodes to produce a surface discharge. The power into the torch is 60 W. The driving gas is argon and the flow rate varies in the range of 3–12 L min^{-1}. Fundamental research results describing the major features of the flow fields induced by the plasma torch are provided in the present study. The stress is laid on the investigation of the influence of gas flow rate, which is one of important operation conditions, on the flow fields excited by the plasma torch. The principal results show that as the power input is fixed the increase of the gas flow rate will reduce the plasma temperature. The plasma penetration length stretching toward the atmospheric surroundings is also found to be closely related with the gas flow rate. Experimental confirmation by measuring the rotational temperature using optical spectroscopic method has been carried out, and a reasonable agreement between calculation and experiment has been obtained. These results provide fundamental understanding of the thermofluid fields induced by a pen-like atmospheric plasma torch, and also build up a basic predictive capability by numerical simulations to perform the further detailed investigation for practical applications in future.

Keywords: Numerical simulation; Plasma torch; Surface treatment; Rotational temperature; Optical spectroscopic method

1. Introduction

The atmospheric pressure plasma can be produced through various types of discharge such as corona discharge, surface discharge, barrier discharge and their combinations. Since the expensive vacuum equipment is not necessary and the radical density is much higher in atmospheric environment, the efficient treatment of materials can be expected by using the atmospheric pressure plasma. The atmospheric pressure plasma has been widely applied to the surface treatment for removal of adsorbates on the substrate before coating [1,2], anti-bacteria [3] and the improvement of the hydrophilic property of the materials [4]. However, for all the atmospheric plasma devices mentioned above, the material being treated is usually exposed to the discharging space. The direct impact and violent bombardment of the active ion species on the material surface will easily cause serious damage, especially for the material with weak strength, such as plastic films. In addition, the precise control to avoid the damage from the high temperature in the reactor is very difficult when treated material locates in the discharging space. For these reasons, the torch type plasma seems useful to be used for material surface treatment because of the material can be placed downstream of the flow to avoid such damages mentioned above. In 2002, an atmospheric plasma device, which was called the pen-like atmospheric plasma torch device with low input power, was proposed by Takayama et al. [4]. The torch was designed to perform the surface treat-

* Corresponding author at: Department of Mechanical Engineering, Lunghwa University of Science and Technology, 300, Wan-Shou Rd. Sec. 1, Kueishan, 33306 Taoyuan, Taiwan. Tel.: +886 2 82093211; fax: +886 2 82091475.
E-mail address: thko@mail.lhu.edu.tw (T.H. Ko).

1290-0729/$ – see front matter
doi:10.1016/j.ijthermalsci.2005.10.007

Nomenclature

$\vec{A}$	vector potential
$\vec{B}$	magnetic flux density
C_υ	specific heat at constant volume
$C_\mu, C_{\varepsilon 1}, C_{\varepsilon 2}$	turbulent model constants
D_f	molecular diffusivity of fuel ..... $m^2\,s^{-1}$
$\vec{E}$	electric field intensity
e	stagnant internal energy per unit volume
e_{ij}	strain rate tensor
$\vec{F}$	Lorentz force
f_{RF}	frequency of RF power supply
G	generation rate of turbulent kinetic energy
i	imaginary unit, respectively
$\vec{j}$	electron current density
P	pressure
$Pr_\kappa, Pr_\varepsilon$	Prandtl numbers
Q	flow rate
Q_j	Joule heating rate
Q_r	radiation energy loss
r	radial coordinate
T	temperature
$\vec{V}$	velocity vector
x	axial coordinate
Y_{air}	concentration of air
Y_{Ar}	concentration of argon

Greek symbols

Γ_κ	transport coefficients for the turbulent kinetic energy κ
Γ_ε	transport coefficients for dissipation rate of turbulent kinetic energy
δ_{ij}	Kronecker delta
ε	dissipation of turbulent kinetic energy
κ	turbulent kinetic energy
λ	thermal conductivity
μ_0	permeability of vacuum
μ_{eff}	effective viscosity
μ_l	laminar viscosity
μ_t	turbulent viscosity
ρ	density
σ	electrical conductivity
$\bar{\bar{\tau}}$	viscous stress
Φ_D	dissipation loss
ω	angular frequency

ment on the plastic film in order to improve its hydrophilic property and produce successful printing on the film. The device has very simple structure and can overcome the defects of traditional atmospheric plasma device for surface treatment as described above. It can be freely moved above the material surface being treated. The distance between the plasma torch and the material surface can also be easily adjusted for obtaining the optimal treating performance. The new device has been tested on the surface treatment for plastic film [4] and polyethylene [5] by using DC or RF power supply. The torch of DC power supply requires high voltage more than 3 kV, but the input power was less than 5 W. However, for the case of RF power supply, the input power could increase easily up to 100 W. From the tests, the treatment by the pen-like atmospheric plasma torch has been verified to have very good performance in improving the hydrophilic properties of materials. The contact angle was effectively reduced from 85.1 deg to 5.5 deg after treatment by using RF power supply [5], and from 50 deg to 5 deg after treatment by DC power supply [4]. The saturated recovery angle after several days of treatment was also satisfactorily smaller than the original values. Because of simple configuration and good treating performance, the device has great potential to become powerful equipment for surface treatment in future. Nonetheless, practical applications require large effective treating area. So far, the effective treating area of a single pen-like atmospheric plasma torch is still too limited to meet the practical requirement. Therefore, further investigation to improve the effective treating area such as by multi-array of the pen-like plasma torch is very necessary.

The factors influencing the hydrophilic properties of material surface are very complicated. Several surface properties, including the roughness and hydrophilic functionalities on the material surface, have been verified to be closely related to the hydrophilic property [5]. The changes of these surface properties are attributed to the bombardment of active radical on the material surface during the plasma treatment process. All of these factors are also believed to be significantly influenced by the flow features induced by the plasma torch. Accordingly, to understand the detailed information of the flow fields induced by the plasma torch would be helpful to find out the relationship between the spatial distribution of gas temperature as well as the flow feature and the change of the surface property. In turn, the optimal operating conditions of the device to increase the effective treating area can be detected from the results. In view of this, the present study intends to build up the mathematical model and perform the numerical simulation to investigate the detailed flow field induced by the pen-like atmospheric plasma torch as a basic step for finding a way by multi-array of the torch to improve the effective treating area of the device. For validating the numerical results, an experimental confirmation by measuring the rotational temperature using the optical spectroscopic method has been carried out and the data will be presented and compared with the calculated gas temperature. In addition, the effects of gas flow rate on the flow field will be analyzed in this paper.

2. Physical model

Fig. 1 shows the configuration of the pen-like atmospheric plasma torch device. A small cylindrical stainless steel pipe

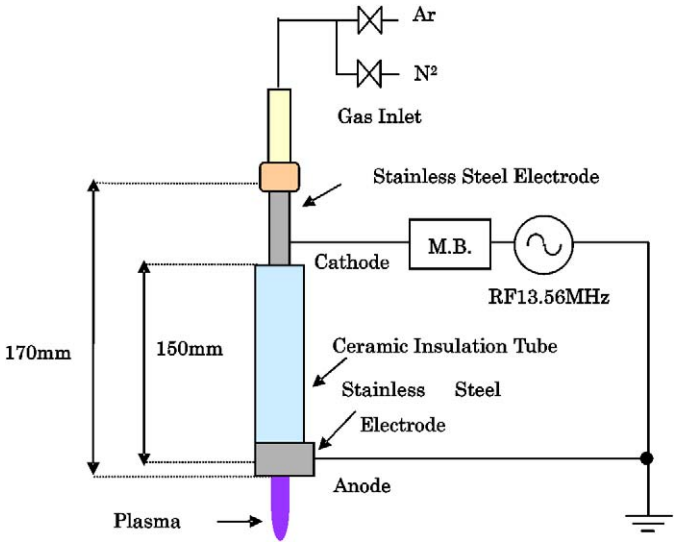

Fig. 1. Configuration of the pen-like atmospheric plasma torch device.

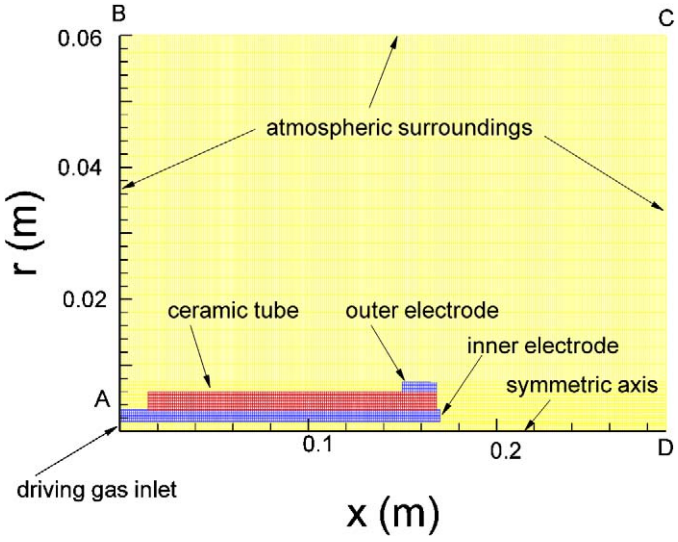

Fig. 2. The 2D computational domain of the pen-like atmospheric plasma torch (unscaled in x- and r-axis).

with 6.5 mm diameter and 170 mm length is inserted as the inner electrode into a ceramic tube of 12 mm diameter and 150 mm length. A ring outer electrode with 15 mm length made of stainless steel is fixed at near the edge of the ceramic. The 13.56 MHz RF power was applied between the two electrodes to produce a surface discharge along the ceramic surface from outer electrodes to the tip of the inner electrodes. The driving gas of Ar was put flow through the center hole of the inner electrode and a torch-like corona plasma will be driven out downstream. The configuration is the same as those studied by Takayama et al. [4] and Lee et al. [5].

3. Mathematical model

3.1. Governing equations

The mathematical model of the present plasma flow system is proposed on the following assumptions: flow, temperature and electromagnetic fields are 2D axisymmetric; flow is steady and isotropic turbulent; all fluids are Newtonian. The local thermodynamic equilibrium (LTE) is assumed in order to simplify mathematical formulation. As a consequence, the plasma is treated as a single continuous fluid with only one representative temperature for the flow. Since the density of free electron is negligibly minor compared with that of heavy particle under atmospheric surroundings, the LTE assumption is generally accepted in the modelling of atmospheric plasma jet [6,7]. Although it is questionable in the very limited region adjacent to the electrode ends where the temperature gradient is very steep, the assumption is valid for most regions in the flow fields. In addition, since the gas components in the current problem are mainly composed of argon and air, the concentrations of argon and air are calculated. All the fluid properties are calculated according to the concentrations of argon and air. The 2D computational domain, as shown in Fig. 2, consists of solid and fluid parts. The solid parts include the inner, outer electrodes as well as the ceramic tube, whereas the fluid part consists of argon issuing from the entrance of inner electrode and air in the surroundings. Thermal energy transport can occur across solid–fluid interfaces in the current problem. Based on the assumptions, the governing equations for the gas flow are presented as follows:

(a) *Continuity equation*:

$$\nabla \cdot (\rho \vec{V}) = 0 \tag{1}$$

where ρ is fluid density; $\vec{V}$ is velocity vector.

(b) *Momentum equations*:

$$\nabla \cdot (\rho \vec{V} \vec{V}) = -\nabla P + \nabla \cdot \bar{\bar{\tau}} + \vec{F} \tag{2}$$

where P is pressure; $\bar{\bar{\tau}}$ is viscous stress: $\bar{\bar{\tau}} = \tau_{ij} = 2\mu_{\text{eff}}(e_{ij} - \frac{1}{3}\delta_{ij}(\nabla \cdot \vec{V}))$; e_{ij} and δ_{ij} are strain rate tensor and the Kronecker delta, respectively; μ_{eff} is the effective viscosity, equal to the summation of laminar viscosity (μ_l) and turbulent viscosity (μ_t); $\vec{F}$ is Lorentz force.

(c) *Concentration equation for* Ar:

$$\frac{\partial}{\partial x_j}(\rho Y_{\text{Ar}} U_j) = \frac{\partial}{\partial x_j}\left[\left(\rho D_f + \frac{\mu_t}{\sigma_f}\right)\left(\frac{\partial Y_{\text{Ar}}}{\partial x_j}\right)\right] \tag{3}$$

where D_f and σ_f are molecular diffusivity and Schmidt number of argon. The air concentration is calculated as: $Y_{\text{air}} = 1 - Y_{\text{Ar}}$.

(d) *Turbulent model*:

The standard κ–ε two equation model is used as turbulent model. The κ–ε equations are:

$$\nabla \cdot (\rho \vec{V} \kappa) = \nabla \cdot (\Gamma_\kappa \nabla \kappa) + G - \rho\varepsilon \tag{4}$$

$$\nabla \cdot (\rho \vec{V} \varepsilon) = \nabla \cdot (\Gamma_\varepsilon \nabla \varepsilon) + C_{\varepsilon 1} G \frac{\varepsilon}{\kappa} - C_{\varepsilon 2} \rho \frac{\varepsilon^2}{\kappa} \tag{5}$$

where $\Gamma_\kappa = \mu_l + \mu_t/Pr_\kappa$, $\Gamma_\varepsilon = \mu_l + \mu_t/Pr_\varepsilon$, are the combined transport coefficients for the turbulent kinetic energy κ and its dissipation rate ε, respectively; μ_t is turbulent viscosity: $\mu_t = \rho C_\mu \kappa^2/\varepsilon$; Pr_κ and Pr_ε are the corresponding Prandtl numbers. G is the generation rate of turbulent kinetic energy.

The constants in the above equations are as follows: $C_\mu = 0.9$, $C_{\varepsilon 1} = 1.44$, $C_{\varepsilon 2} = 1.92$, $Pr_\kappa = 1.0$, $Pr_\varepsilon = 1.3$, $\sigma_f = 0.5$.

(e) *Energy equation*:

$$\nabla \cdot \left[(e+P)\vec{V}\right] = \nabla \cdot (\lambda \nabla T) + \Phi_D + Q_j - Q_r \tag{6}$$

where T is temperature; e is stagnant internal energy per unit volume:

$$e = \rho\left(C_\upsilon T + \frac{\vec{V}\cdot\vec{V}}{2}\right)$$

Φ_D is dissipation loss:

$$\Phi_D = 2\mu_{\text{eff}}\left(e_{ij} - \frac{1}{3}\delta_{ij}(\nabla\cdot\vec{V})\right)^2$$

Q_j is Joule heating rate: $Q_j = \vec{j}\cdot\vec{E}$. Q_r is radiation energy loss. The discrete ordinate method developed by Fiveland [8] is employed to calculate Q_r. $\vec{E}$ is electric field intensity; $\vec{j}$ is electron current density; C_υ is specific heat at constant volume; σ is electrical conductivity; λ is thermal conductivity.

(f) *Equation of state*:

$$P = \rho RT \tag{7}$$

(g) *Vector potential equation*:

For electromagnetic field, the vector potential equation, which was presented by Mostaghimi and Boulos [9], is derived from Maxwell's equation:

$$\nabla^2\vec{A}_C - i\mu_0\sigma\omega\vec{A}_C = 0 \tag{8}$$

(h) *Electric field*:

$$\vec{E}_C = -i\omega\vec{A}_C \tag{9}$$

(i) *Magnetic field*:

$$\vec{B}_C = \nabla\times\vec{A}_C \tag{10}$$

where $\omega = 2\pi f_{\text{RF}}$, $\vec{A}(\vec{r},t) = \vec{A}_C(\vec{r})e^{i\omega t}$, $\vec{B}(\vec{r},t) = \vec{B}_C(\vec{r})e^{i\omega t}$, $\vec{E}(\vec{r},t) = \vec{E}_C(\vec{r})e^{i\omega t}$. In the equations, $\vec{A}$ is vector potential; $\vec{E}$ is electric field intensity; $\vec{B}$ is magnetic flux density; f_{RF} is frequency of RF power supply; ω is angular frequency; μ_0 and i represent permeability of vacuum and imaginary unit, respectively. The electric current density is calculated as $\vec{j} = \sigma\vec{E}$.

3.2. Boundary conditions

The computational domain is shown as Fig. 2, in which the boundary lines of A-B, B-C and C-D are selected as far enough for setting the atmospheric conditions there. The boundary conditions for mass, momentum and energy equations are as follows: the symmetric conditions are imposed on the axis of symmetry. On the boundary lines, including A-B, B-C and C-D (see Fig. 2), the flow conditions are assumed as fixed pressure. Non-slip condition is considered on all solid walls. Traditional wall function is employed in the near wall regions to avoid the requirement of the dense grids. At inlet, the uniform velocity profile is assumed and the velocity magnitude is determined according to the gas flow rate. The temperature and Y_{Ar} of flow-in gas are 300 K and 1.0, respectively. The boundary conditions for the vector potential are: on the axis of symmetry, vector potential is assumed zero. At boundary lines A-B, B-C and C-D, there is no gradient existence. Between the anode and cathode, the RF power supply is added. The power supply is fixed as 60 W.

3.3. Numerical methods

The governing Eqs. (1)–(7) with auxiliary Eqs. (8)–(10) and the described boundary conditions are discretized by a finite volume formulation. In the equations, the convective terms are modeled by the secondary-order upwind scheme; meanwhile the diffusive terms are modeled by the central difference scheme. The numerical solution procedure adopts the well-known semi-implicit SIMPLE algorithm, which was developed by Launder and Spalding [10]. All the detailed numerical procedure can be found in the book of Patankar [11]. The element number is 12 839. The convergent tolerance is set as the global normalized residues in the whole computational domain of every solved variable are less than 10^{-4}. A commercial CFD software CFD RC (ESI US R&D, Inc.) is used for the numerical solutions.

4. Experimental setup and measurement method

The rotational temperature of nitrogen molecules usually can be taken as the gas temperature because of many collisions occur within the gas molecules under atmospheric pressure conditions. So that, for validating the numerical results, the axial distribution of the rotational temperature along the gas flow was measured using spectroscopic method for comparison with the gas temperature theoretically calculated. Fig. 3 shows the block diagram of the experimental system used. The light emitted from the plasma is collected by an optical fiber connected with the multi-channel spectroscope. The analyzed optical spectrum are detected by a CCD system, transferred into electrical signals using the photo-multi-amplifier (PMA) and finally recorded by the personal computer.

Fig. 4(a) shows the typical spectrum experimentally obtained. These spectrum belong to N_2 second positive bands $C^3\pi_u(v') \rightarrow B^3\pi_g(v'')$, each peak corresponds to the transition

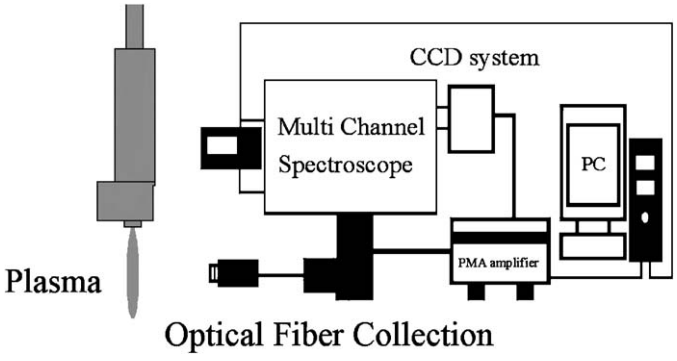

Fig. 3. Block diagram of the experimental system for measuring the vibrational temperature.

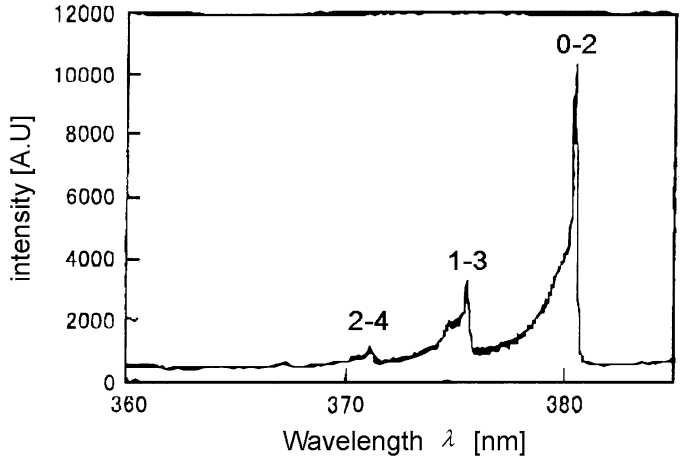

(a)

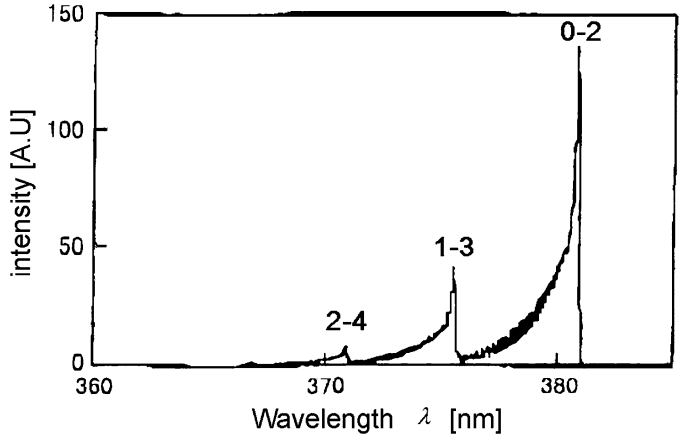

(b)

Fig. 4. Comparison between typical example of the optical spectrum obtained by experimental and by calculation: (a) Experimental spectrum. Power = 60 W, $Q = 5\ \mathrm{L\,min^{-1}}$; (b) Calculated spectrum. $T_{\mathrm{rot}} = 900$ K, $T_{\mathrm{vib}} = 1800$ K.

of vibrational quantum number $\Delta v = v' - v'' = -2$, that is, transition from the upper level $C(v' = 0)$ to the lower level $B(v'' = 2)$, $v' = 1$ to $v'' = 3$ and $v' = 2$ to $v'' = 4$, respectively.

Due to the insufficient resolution ability of the spectroscope and also because of the rotational temperature was rather high (approximately 1000 K) in this experiment, the rotational spectrums are always overlapped on the vibrational spectrum as shown in Fig. 4(a). For obtaining an exact value of rotational temperature without influence of the overlapping of the spectrum, the experimental spectrum are compared with theoretical spectrum which are calculated for a given vibrational temperature T_{vib} and a rotational temperature T_{rot} by taking into account the device factor used [12]. An example of the calculated spectrum using $T_{\mathrm{rot}} = 900$ K and $T_{\mathrm{vib}} = 1800$ K for the spectroscope used in the present experiment are shown in Fig. 4(b). By best fitting of the experimental spectrum with the calculated, a best fitted rotational temperature simultaneously with vibrational temperature can be finally obtained. Through a series of analysis, the uncertainty of the current measurements is 8%.

5. Results and discussion

5.1. Comparison of numerical results and experimental data

Fig. 5 presents a photo of plasma torch produced by the pen-like plasma torch device in the laboratory, in which the plasma gas flow can be very clearly observed from the end-tip of the inner electrode. In the photo, a piece of carbon included polyethylene to be treated was placed at downstream of the plasma flow. From the view point of practical applications, the understanding of the characteristics of plasma from the end-tip of inner electrode toward downstream is the major concern; therefore, the following discussion will focus on the flow fields in the downstream region from the end-tip of the inner electrode. Numerical results and experimental data of temperature distributions along the central line of corona torch are compared first to verify the accuracy of numerical predictions. The compared cases include two operating conditions with different flow rates of driving gas. The two cases are Power = 60 W, $Q = 5\ \mathrm{L\,min^{-1}}$; and Power = 60 W, $Q = 9\ \mathrm{L\,min^{-1}}$. The comparisons are shown in Figs. 6(a) and (b), respectively. In the figures, the starting point of x-axis, which locates at $x = 170$ mm, is the end-tip position of the inner electrode in the pen-like plasma device, as shown in Fig. 1. From the figures, it can be found that the numerical predictions of both cases are very accurate in the upstream region, whereas some difference exists in the downstream. The difference is attributed to numerical errors, but it is also believed to be resulted from the uncertainty of the experimental measurements. From the observation of the experiments, the light of the pen-like corona torch is found to become weaker very quickly as the flow develops toward downstream. The weak light is detrimental for the precise measurement since the measuring method is principally based on the brightness of the light. Besides, the strong mixing of the plasma gas with surrounding air and the small Joule heating in the downstream are also the factors to cause the deviation between numerical predictions and measurements. Nonetheless, the maximum difference between the numerical predictions and experimental results for the two cases is less than 24%. From the viewpoint of practical applications, the current numerical predictions show reasonable accuracy.

5.2. Flow fields analysis of a baseline case

For understanding the flow fields excited by the corona discharge in the pen-like plasma torch, a baseline case with Power = 60 W and $Q = 5\ \mathrm{L\,min^{-1}}$ is investigated and analyzed in detail. Fig. 7 shows the temperature distribution (upper part) and axial velocity contours (lower part) for the baseline case. The highest temperature in this case is about 950 K, which occurs in a very limited region close to the end-tip of the inner electrode. The penetrated positions of the corona torch with 900 K, 800 K and 700 K are about $x = 177$ mm, 182 mm and 200 mm, respectively in axial direction; and $r = 0.68$ mm, 1.2 mm and 1.8 mm, respectively in radial direction. The rapid change and decrease of the gas temperature in both axial and radial directions is attributed to the entrainments of cold air as the

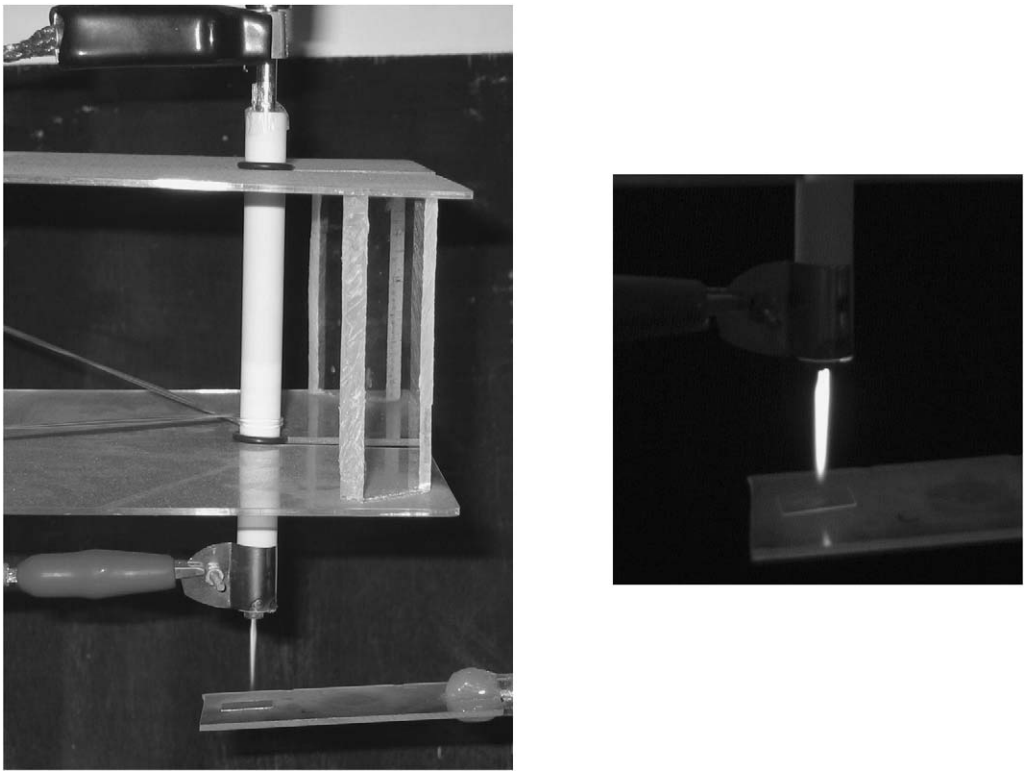

Fig. 5. The plasma torch produced by the pen-like plasma torch device in laboratory.

corona gas jet issues into the atmospheric surroundings. Since the cold air greatly reduces the gas temperature and influences the plasma quality significantly, the amount of the entrained cold air requires special caution, and will be discussed in the following. From the axial velocity contours, as shown in the lower part of Fig. 7, the gas velocity is found to be raised considerably, which is caused by the great increase of gas temperature and the influence of Lorentz force near the end-tip of the inner electrode. The velocity of driving gas at the inner electrode entrance is 11.8 m s^{-1} for the current case, and the maximum axial velocity near the exit of inner electrodes is found to be accelerated to reach 40.0 m s^{-1}, which is nearly 3.4 times of the magnitude at the electrode entrance. However, the plasma gas velocity decays very fast as the gas jet issues into the surroundings. In axial direction, the penetration depth of the region with velocity larger than inlet velocity extends to the position about $x = 209.4$ mm, after which the gas velocity decreases to the magnitude lower than the inlet velocity. The figure also indicates the momentum transport of the gas jet in the radial direction, from which it can be found that the high-velocity flow zone is limited in a very small region. The radial location with axial velocity larger than inlet velocity concentrates only in a very narrow core with radius smaller than $r = 2.2$ mm. Beyond the radial region, the velocity decays with a very steep gradient. Fig. 8 shows the radial velocity contours (upper part) and velocity vector plots as well as streamlines (lower part) for the baseline case, from which the entrainment of the cold air from atmospheric surroundings can be detected. Near the central axis of the corona torch, the radial velocity is positive, which indicates the flow is expanding toward the outer region. Such result

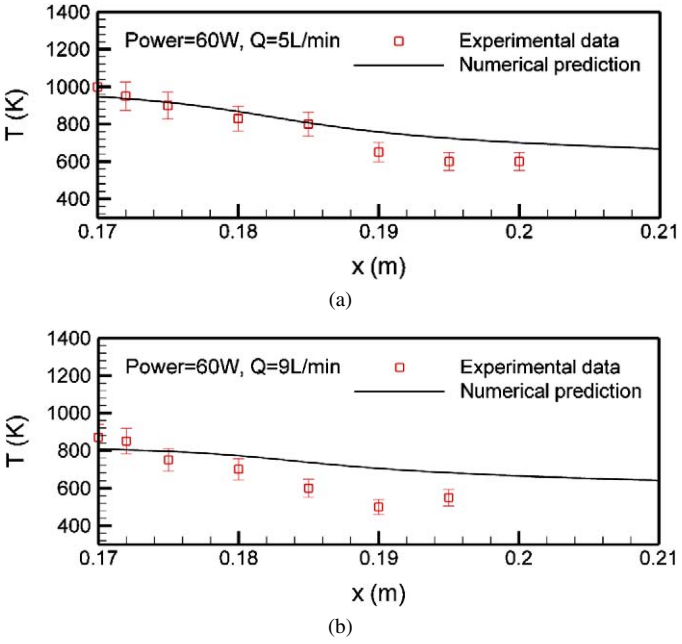

Fig. 6. Comparison of numerical prediction and experimental results of temperature distribution along central axis: (a) Power = 60 W, $Q = 5$ L min^{-1}; (b) Power = 60 W, $Q = 9$ L min^{-1}.

is caused by the expansion effect of the high-temperature gas near the central region. However, the positive radial velocity is very minor; the maximum of the positive radial velocity is only 0.4 m s^{-1}. The radial velocity becomes negative around the central regions, which indicates the fluid is sucked toward the central zone from surroundings. The result is due to the rel-

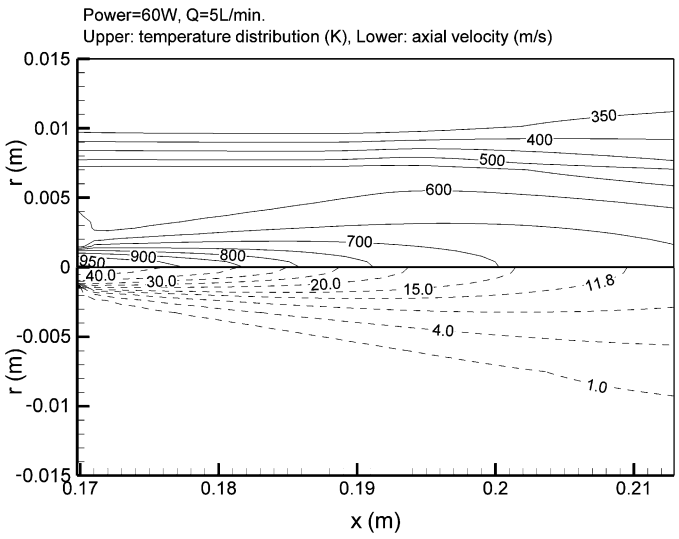

Fig. 7. The temperature distribution (upper part) and axial velocity contours (lower part) for case with Power = 60 W and $Q = 5\ \mathrm{L\,min^{-1}}$.

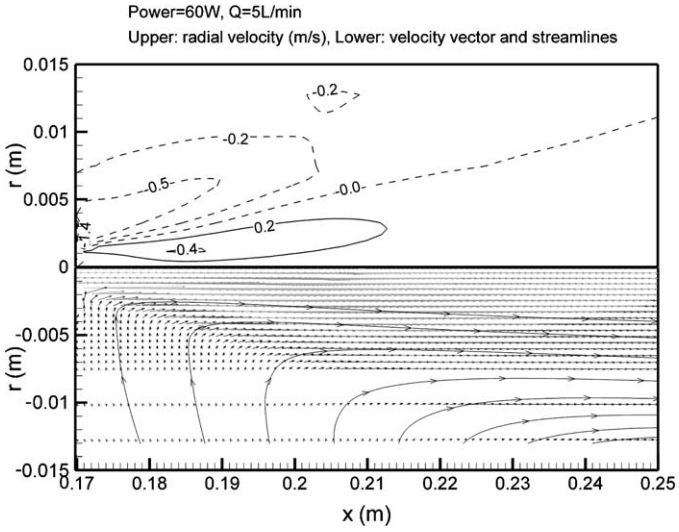

Fig. 8. The radial velocity contours (upper part) and velocity vector and streamlines (lower part) of case with Power = 60 W and $Q = 5\ \mathrm{L\,min^{-1}}$.

atively low pressure field formed in the region near the central axis caused by the issuing of high-velocity jet, and in turn the cold air in atmospheric surroundings will be sucked into the region near the central axis. Since the entrained cold air will greatly reduce the corona temperature and influence the plasma quality, the amount of the entrained air should be controlled as lower as possible. For the current baseline case, the maximum of the negative radial velocity is $-1.4\ \mathrm{m\,s^{-1}}$, which is much larger than the positive radial velocity.

5.3. Effects of driving gas flow rate

For understanding the effects of driving gas flow rate on the flow filed accompanied with the corona torch, the following will compare the calculated results of $Q = 3\ \mathrm{L\,min^{-1}}$ and $12\ \mathrm{L\,min^{-1}}$ cases. The power of both cases is fixed as 60 W. Fig. 9 shows the temperature contours for the two different flow

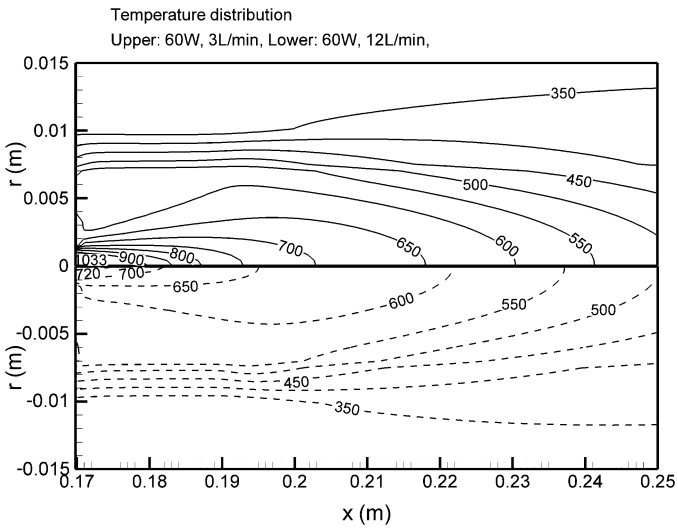

Fig. 9. The comparison of temperature distributions in cases with Power = 60 W, $Q = 3\ \mathrm{L\,min^{-1}}$ (upper part) and Power = 60 W, $Q = 12\ \mathrm{L\,min^{-1}}$ (lower part).

rate cases, in which the upper and lower part are $Q = 3\ \mathrm{L\,min^{-1}}$ and $12\ \mathrm{L\,min^{-1}}$, respectively. For both cases, the basic patterns of temperature distribution are very similar, in which the highest temperature occurs in central core of the torch, and the temperature decreases very fast along axial as well as radial directions. As the flow rate increases, the gas temperature is found to decrease significantly. The highest temperature in $Q = 3\ \mathrm{L\,min^{-1}}$ case is about 1033 K, whereas the highest temperature reduces to 720 K in $Q = 12\ \mathrm{L\,min^{-1}}$ case. In addition, the penetration region of the fluid with higher temperature becomes smaller in both axial and radial directions as the flow rate increases. In $Q = 3\ \mathrm{L\,min^{-1}}$ case, the high-temperature gas above 700 K is found to extend up to $x = 203$ mm and $r = 2.1$ mm in axial and radial direction, respectively, which are both wider than those in $Q = 5\ \mathrm{L\,min^{-1}}$ case as mentioned previously. In the case with Q increases to $12\ \mathrm{L\,min^{-1}}$, the gas flow with temperature above 700 K is greatly reduced to the position of $x = 182$ mm and $r = 0.7$ mm in axial and radial direction, respectively. Fig. 10 shows the comparison of the axial temperature distributions along the central axis for the cases with different driving gas flow rates, which clearly indicates the fast decay of the plasma gas temperature; meanwhile, the obvious reduction of the plasma gas temperature will be resulted as driving gas flow rate increases. These changes point out the important influence of driving gas flow rate on the flow fields of plasma torch, which is worthwhile information for practical applications. The comparison of the axial velocity distribution with different driving gas flow rates are shown in Fig. 11. The driving gas velocities at the entrance of inner electrode for $Q = 3\ \mathrm{L\,min^{-1}}$ and $12\ \mathrm{L\,min^{-1}}$ cases are $7.074\ \mathrm{m\,s^{-1}}$ and $28.296\ \mathrm{m\,s^{-1}}$, respectively. For both cases, the plasma gas is found to be considerably accelerated. Similar with the situations in the baseline case with $Q = 5\ \mathrm{L\,min^{-1}}$, the highest velocity appears in the region very close to the end-tip of the inner electrode, and decays with a very quick speed as the flow develops along the downstream. The high-

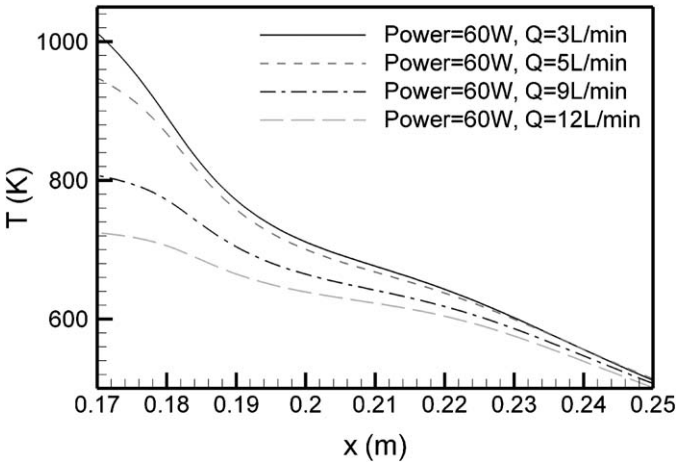

Fig. 10. Comparison of temperature distributions along central axis of plasma torch for Power = 60 W cases with $Q = 3$ L min^{-1}, 5 L min^{-1} and 12 L min^{-1}.

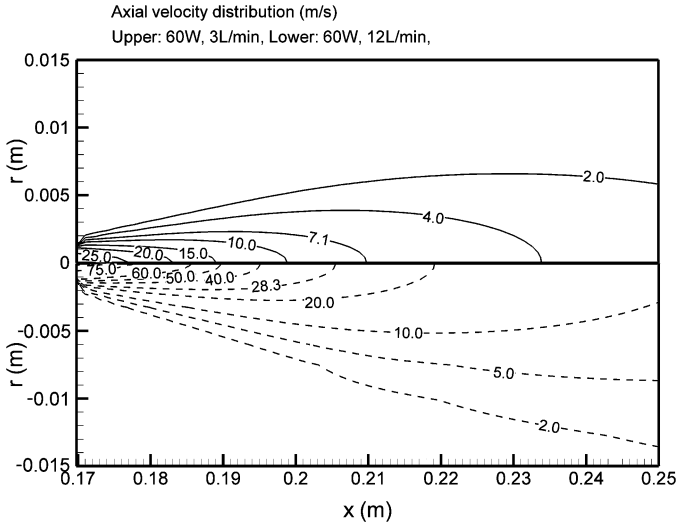

Fig. 11. The comparison of axial velocity distributions of cases with Power = 60 W, $Q = 3$ L min^{-1} (upper part) and Power = 60 W, $Q = 12$ L min^{-1} (lower part).

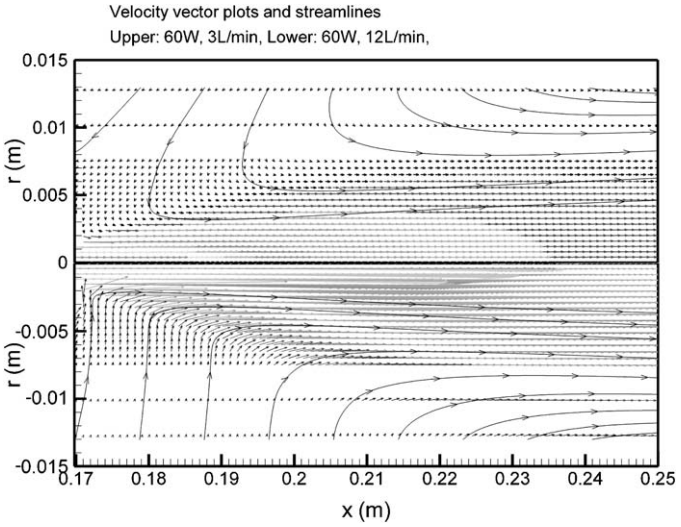

Fig. 12. The comparison of velocity vectors and streamlines of cases with Power = 60 W, $Q = 3$ L min^{-1} (upper part) and Power = 60 W, $Q = 12$ L min^{-1} (lower part).

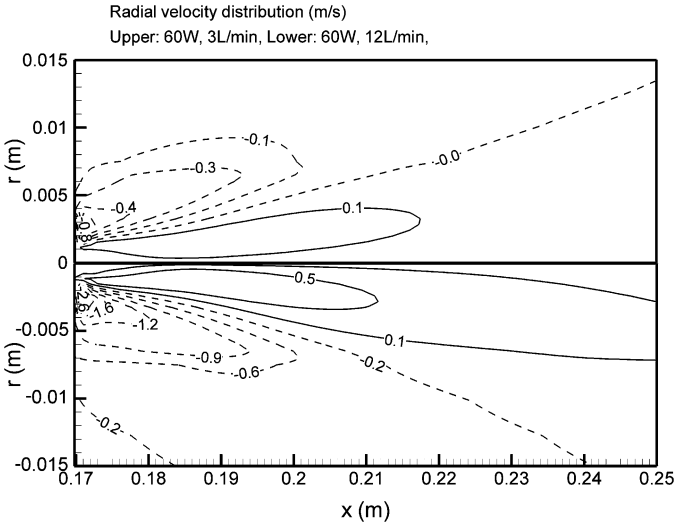

Fig. 13. The comparison of radial velocity contours of cases with Power = 60 W, $Q = 3$ L min^{-1} (upper part) and Power = 60 W, $Q = 12$ L min^{-1} (lower part).

est axial velocities in $Q = 3$ L min^{-1} and 12 L min^{-1} cases are 25 m s^{-1} and 75 m s^{-1}, respectively, which are about 3.8 and 2.75 times of the corresponding driving gas velocity at inner electrode entrance, respectively. Including the consideration of previous discussion in $Q = 5$ L min^{-1} case, which shows the highest axial velocity is 3.5 times of the driving gas velocity at inner electrode entrance, the acceleration is found to be more serious in cases with lower driving gas flow rate. Such results are attributed to the higher temperature rise in the lower flow rate cases, as been discussed previously. Since the original velocities of driving gas at inner electrode entrance are different in the cases with different driving gas flow rates, the comparison of the penetration depth of plasma gas flow will be based on the penetrating position of the fluid with velocity equal to the inlet velocity at inner electrode entrance for the corresponding flow rate case, i.e. 7.1 m s^{-1} and 28.3 m s^{-1} for $Q = 3$ L min^{-1} and 12 L min^{-1} cases, respectively. From the figure, the penetration position is $x = 209.8$ mm in $Q = 3$ L min^{-1} case, which is larger than 205.5 mm in $Q = 12$ L min^{-1} case. The results indicate the penetration depth reduces as the driving gas flow rate increases. Figs. 12 and 13 show the velocity vector plots as well as streamlines and radial velocity contours for $Q = 3$ L min^{-1} and 12 L min^{-1} cases, respectively. Similar with the baseline case, the radial velocity near the central axis is positive, which indicates the fluid in the region tends to expand toward outside. In the surrounding region around the central axis, the cold air is entrained into the central core; therefore, the radial velocity is negative. The maximum of the negative radial velocity for $Q = 3$ L min^{-1} and 12 L min^{-1} cases is -0.8 m s^{-1} and -2.6 m s^{-1}, which indicates the increase of the driving gas flow rate will cause the more cold air to be entrained from the surroundings into the flow central core, which is detrimental for the plasma quality. The contours of air concentration for the cases with $Q = 3$ L min^{-1} and 12 L min^{-1} are shown in Fig. 14, from

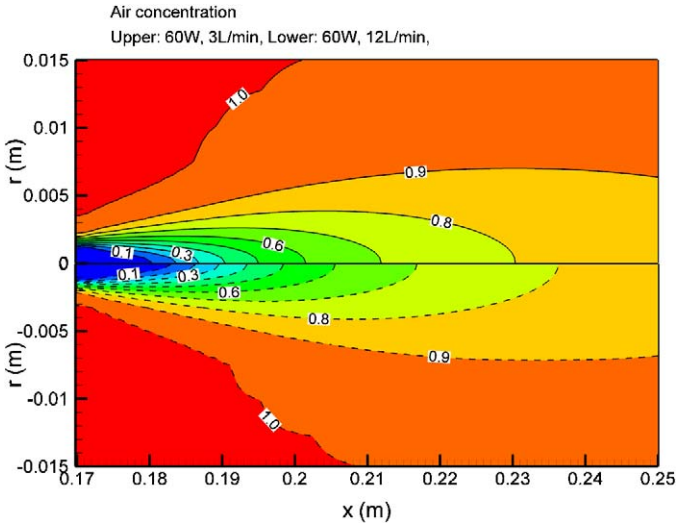

Fig. 14. The comparison of air concentration contours of cases with Power = 60 W, $Q = 3\ \mathrm{L\,min^{-1}}$ (upper part) and Power = 60 W, $Q = 12\ \mathrm{L\,min^{-1}}$ (lower part).

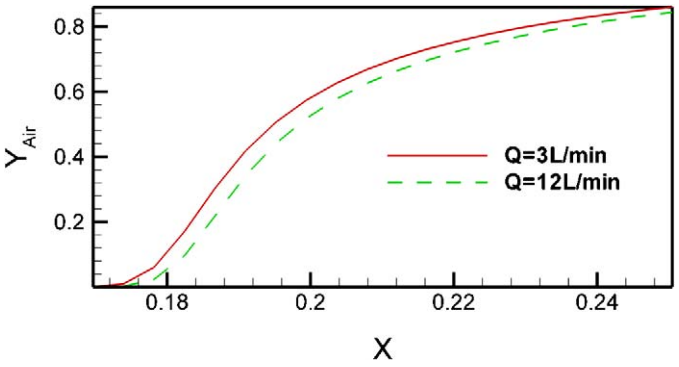

Fig. 15. The comparison of air concentration along central axis of plasma torch for cases with Power = 60 W, $Q = 3\ \mathrm{L\,min^{-1}}$ and Power = 60 W, $Q = 12\ \mathrm{L\,min^{-1}}$.

which the entrainment of air from surroundings can be detected. Basically, the distribution patterns of the air concentration for the two cases are very similar. The air concentration increases gradually from 0.1 near the inner electrode exit to 1.0 along both of axial and radial directions. Fig. 15 shows the air concentration along the central axis of the plasma torch, from which the air concentration of $Q = 3\ \mathrm{L\,min^{-1}}$ case can be found a little higher than that in $Q = 12\ \mathrm{L\,min^{-1}}$ case. The maximum difference is about 35.7%. However, since the flow rate of argon in $Q = 12\ \mathrm{L\,min^{-1}}$ case is four times of that in $Q = 3\ \mathrm{L\,min^{-1}}$ case, it can be judged the amount of air being sucked into the plasma jet is much larger in the $Q = 12\ \mathrm{L\,min^{-1}}$ case.

6. Conclusions

The present paper investigates the thermofluid fields excited by the pen-like atmospheric plasma torch with numerical simulations as well as experimental methods. The results provide fundamental understanding on the behavior of the pen-like atmospheric plasma torch, especially on the resulted gas temperature, and also build up a basic predicted capability to perform further detailed investigation in future. Information about the gas temperature is useful for practical application of the plasma torch because the gas temperature may relate to the formation of active radicals which will play an important role in the material processing. Through comparisons between the numerical results and experimental data, the numerical simulation is verified to have reasonable accuracy. The principal conclusions are as follows.

(1) From both of numerical and experimental results, a torch-like corona plasma can be found to be driven out from the end-tip of inner electrode in the device, and tends to stretch toward the atmospheric surroundings. The highest temperature in the plasma torch occurs in a very limited region close to the end-tip of the inner electrode.
(2) In both of axial and radial directions, the temperature decays with a very steep gradient, which is caused by the entrainments of cold air from atmospheric surroundings into plasma central core as the gas jet issues into the flow field. The entrained cold air will significantly reduce the gas temperature and velocity.
(3) Due to the temperature rise, the plasma gas velocity is considerably accelerated near the end-tip of the inner electrode, but also decays very fast as the gas jet issues into the surroundings. The increase of driving gas flow rate will reduce the plasma temperature. The highest temperatures of plasma gas for $Q = 3\ \mathrm{L\,min^{-1}}$, $5\ \mathrm{L\,min^{-1}}$ and $12\ \mathrm{L\,min^{-1}}$ cases are 1033 K, 950 K and 720 K, respectively.
(4) Based on the penetrating position of the fluid with velocity equal to the inlet velocity at inner electrode entrance for the respective flow rate case, the penetration depth is found to reduce as the driving gas flow rate increases, which is attributed to the milder temperature rise in the cases with larger driving gas flow rate, and therefore, the acceleration of plasma gas becomes more gentle.
(5) The maximum of negative radial velocity increases in the case with larger driving gas flow rate, indicating the increase of driving gas flow rate will cause more cold air to be entrained from surroundings into the flow central core. Since the entrained cold air will reduce plasma gas temperature and velocity, the control method to prohibit cold air being entrained into plasma central core requires special caution in future design works for practical applications. A solid shield equipped around the pen-like plasma torch, which is like the design used for the atmospheric thermal plasma spraying system [13], is a possible resolution.

The present study accomplished a preliminary work for developing the pen-like atmospheric plasma torch. However, for further attacking the real mechanism to cause the improvement of the hydrophilic property of materials by using the device, the in depth simulations are essentially required. The simulations must include the impingement phenomena between the plasma jet and the treated material surface so that the optimal operating conditions can be investigated. These studies are now being processed by the research team.

Acknowledgements

This work was supported by the National Science Council of Taiwan, ROC (project No. 93-2212-E262-002).

References

[1] B.N. Chapman, Glow Discharge Process Sputtering and Plasma Etching, Wiley, New York, 1980.
[2] K. Pochner, W. Neff, R. Lebert, Atmospheric pressure gas discharges for surface treatment, Surface Coating Technol. 74–75 (1995) 394–398.
[3] T. Akitsu, H. Ohkawa, M. Ohnishi, M. Tsuji, M. Kogoma, A study on anti-bacterial effect of non-thermal oxygen plasma and bio-medical application, in: Proceedings of the 3rd Asia-Pacific International Symposium on the Basic and Application of Plasma Technology, Taiwan, ROC, 2003, pp. 139–144.
[4] S. Takayama, S. Ono, S. Teii, Surface treatment of plastics by an atmospheric pressure corona torch, Trans. IEE Japan A 122 (8) (2002) 722–728.
[5] J.L. Lee, C.M. Liu, K. Ting, W.K. Cheng, S. Takizawa, S. Arase, S. Ono, S. Teii, Plasma treatment of polyethylene surface for metallizing by using an atmospheric pressure corona torch, in: Proceedings of the 3rd Asia-Pacific International Symposium on the Basic and Application of Plasma Technology, Taiwan, ROC, 2003, pp. 237–242.
[6] M. Boulos, P. Fauchais, E. Pfender, M. Mariaux, E. Legros, Thermal Plasma: Fundamental and Applications, Plenum, New York, 1995.
[7] G. Mariaux, A. Vardelle, 3-D time-dependent modelling of the plasma spraying process. Part 1: flow modelling, Int. J. Therm. Sci. 44 (2005) 357–366.
[8] W.A. Fiveland, Three-dimensional radiative heat-transfer solution by the discrete ordinates method, J. Thermodyn. Heat Transfer 2 (4) (1988) 209–316.
[9] J. Mostaghimi, M. Boulos, Two-dimensional electromagnetic field effects in induction plasma modeling, Plasma Chem. Plasma Process 9 (1989) 25–44.
[10] B.E. Launder, D.B. Spalding, The numerical computation of turbulent flows, Comput. Methods Appl. Mech. Engrg. 3 (1974) 269.
[11] S.V. Patankar, Numerical Heat Transfer and Fluid Flow, Hemisphere, New York, 1980.
[12] D.M. Phillips, Determination of gas temperature from unresolved bands in the spectrum from a nitrogen discharge, J. Phys. D: Appl. Phys. 9 (3) (1976) 507–521.
[13] D.T. Gawne, T. Zhang, B. Liu, Computational analysis of the influence of a substrate, solid shield and gas shroud on the flow field of a plasma jet, Surface Coatings Technol. 153 (2002) 138–147.